PNAS RESEARCH ARTICLE | EARTH, ATMOSPHERIC, AND PLANETARY SCIENCES OPEN ACCESS

A weakened AMOC may prolong greenhouse gas–induced Mediterranean drying even with significant and rapid climate change mitigation

Thomas L. Delworth[a,1], William F. Cooke[a], Vaishali Naik[a], David Paynter[a], and Liping Zhang[a,b]

Edited by Clara Deser, National Center for Atmospheric Research, Boulder, CO; received October 15, 2021; accepted June 30, 2022

The Mediterranean region has been identified as a climate hot spot, with models projecting a robust warming and rainfall decline in response to increasing greenhouse gases. The projected rainfall decline would have impacts on agriculture and water resources. Can such changes be reversed with significant reductions in greenhouse gases? To explore this, we examine large ensembles of a high-resolution climate model with various future radiative forcing scenarios, including a scenario with substantial reductions in greenhouse gas concentrations beginning in the mid-21st century. In response to greenhouse gas reductions, the Mediterranean summer rainfall decline is reversed, but the winter rainfall decline continues. This continued winter rainfall decline results from a persistent atmospheric anticyclone over the western Mediterranean. Using additional numerical experiments, we show that the anticyclone and continued winter rainfall decline are attributable to greenhouse gas–induced weakening of the Atlantic Meridional Overturning Circulation (AMOC) that continues throughout the 21st century. The persistently weak AMOC, in concert with greenhouse gas reductions, leads to rapid cooling and sea ice growth in the subpolar North Atlantic. This cooling leads to a strong cyclonic atmospheric circulation anomaly over the North Atlantic subpolar gyre and, via atmospheric teleconnections, to the anticyclonic circulation anomaly over the Mediterranean. The failure to reverse the winter rainfall decline, despite substantial climate change mitigation, is an example of a "surprise" in the climate system. In this case, a persistent AMOC change unexpectedly impedes the reversibility of Mediterranean climate change. Such surprises could complicate pathways toward full climate recovery.

climate | Mediterranean | rainfall | mitigation | AMOC

Significance

The Mediterranean is a projected hot spot for climate change, with significant warming and rainfall reductions. We use climate model ensembles to explore whether these Mediterranean rainfall declines could be reversed in response to greenhouse gas reductions. While the summer Mediterranean rainfall decline is reversed, winter rainfall continues to decline. The continued decline results from prolonged weakening of Atlantic Ocean poleward heat transport that combines with greenhouse gas reductions to cool the subpolar North Atlantic, inducing atmospheric circulation changes that favor continued Mediterranean drying. This is a potential "surprise" in the climate system, whereby changes in one component (Atlantic Ocean circulation) alter how another component (Mediterranean rainfall) responds to greenhouse gas reductions. Such surprises could complicate climate change mitigation efforts.

Projections of changes in regional climate and extremes are vital for planning and decision making over the coming decades and are a critical topic for societally relevant research (1–6). A particularly important question is the extent to which climate change would be reversed if greenhouse gas concentrations were to substantially decline later this century (7, 8). Are there climate system changes that would not be reversed in response to significant reductions in emissions (8–23)? Have any such components crossed thresholds from which recovery may be difficult? We probe these issues by conducting large ensembles of climate change simulations under various forcing scenarios, including future reductions in greenhouse gases. Large ensembles are especially useful for assessing both the mean climate response to radiative forcing changes and the internal variability of the coupled system (24–26). We use a climate model with a high-resolution atmosphere–land component (50 km horizontal resolution) to better simulate changes in regional climate and extremes. We use 30-member ensembles to obtain a robust simulation of both the radiatively forced signal, as expressed by the ensemble mean, and the internal variability as indicated by the spread of the individual members around the ensemble mean. We focus on a regional hot spot for climate change—the Mediterranean—where rainfall declines have been observed (27) and are robustly projected in response to increasing greenhouse gases (28). We assess whether such rainfall declines could be reversed by significant reductions in greenhouse gases beginning in the mid-21st century.

We use a modeling system (SPEAR; **S**eamless System for **P**rediction and **EA**rth system **R**esearch) that is also used for real-time seasonal (29) to decadal predictions (30), with validated skill on those time scales (31), including for predictions of Arctic sea ice extent (32) and the Atlantic Meridional Overturning Circulation (AMOC). We first conduct a natural ensemble that is forced only with estimates of observed changes in solar irradiance and volcanic aerosols over 1921 to 2014, as well as hypothetical variations in solar irradiance and volcanic aerosols over 2015 to 2100 (see *Methods* for details). This ensemble has

Author contributions: T.L.D. designed research; T.L.D. and W.F.C. performed research; T.L.D. and W.F.C. analyzed data; V.N. and D.P. processed the forcings applied in the simulations; and T.L.D., W.F.C., V.N., D.P., and L.Z. wrote the paper.

The authors declare no competing interest.

This article is a PNAS Direct Submission.

[1]To whom correspondence may be addressed. Email: tom.delworth@noaa.gov.

This article contains supporting information online at http://www.pnas.org/lookup/suppl/doi:10.1073/pnas.2116655119/-/DCSupplemental.

Published August 22, 2022.

anthropogenic greenhouse gases, aerosols, and land use fixed at calendar year 1921. This is a reference against which other simulations are compared. We conduct a 30-member historical ensemble of simulations over the period 1921 to 2014 that is driven by observationally based estimates of changes in radiative forcing. The ends of these historical simulations serve as the starting points for simulations over the period 2015 to 2100. We conduct four separate 30-member ensembles using the Shared Socioeconomic Pathways (SSP) scenarios SSP1-1.9, SSP2-4.5, SSP5-8.5, and SSP5-3.4-OS (33) (hereafter referred to as SSP119, SSP245, SSP585, and SSP534OS; *Methods*). The first three scenarios represent very low, medium, and very high estimates of future greenhouse gas emissions (the SSP585 scenario may be viewed as a low-likelihood but high-impact outcome) (34). The fourth scenario, SSP534OS, is especially revealing as it contains rapid increases in greenhouse gases until the mid-21st century (similar to SSP585), after which there is a rapid decline in greenhouse gas concentrations. The SSP534OS scenario helps to assess whether and how rapidly climate change can be reversed.

Radiative Balance, Temperature, and Precipitation Response

We show in Fig. 1*A* the response of simulated annual mean global mean surface air temperature to various scenarios of radiative forcing changes. In all cases the global mean temperature responds within a decade to imposed changing greenhouse gas concentrations (*SI Appendix*, Fig. S1). Note that despite the reversal of the global warming in SSP534OS after 2060, the simulated global mean temperature is still more than 0.5 K warmer in 2100 than in year 2022. The spread of the individual members around the ensemble mean is relatively small for global mean changes. The changes in global mean surface air temperature are consistent with changes in the net radiative balance at the top of the atmosphere (*SI Appendix*, Fig. S2). The

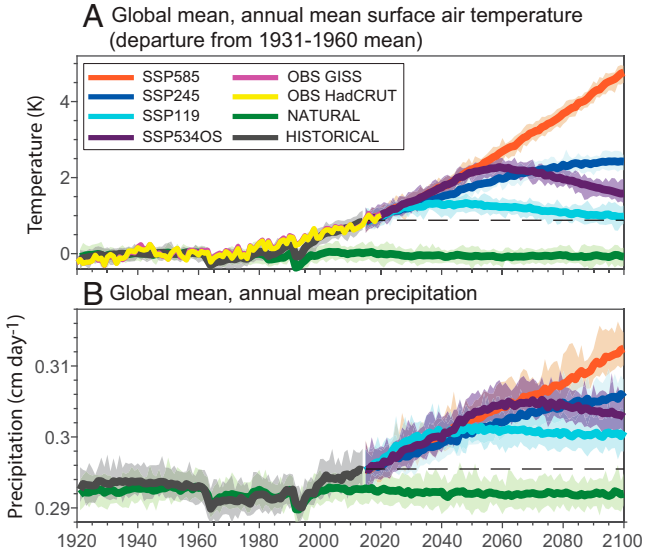

Fig. 1. (*A*) Time series of global mean, annual mean surface air temperature. For all time series in *A*, values plotted are differences with respect to ensemble mean, time mean values over the period 1931 to 1960. Legend in *A* also applies to *B*. The curves labeled "OBS GISS" and "OBS HadCRUT" are observational time series (*Methods*). (*B*) Time series of annual mean, global mean precipitation (units are cm day^{-1}). The thick solid lines in each panel indicate the 30-member ensemble means, while the shaded regions indicate the range of the ensemble members. The dashed black line in each panel indicates the mean value over the period 2011 to 2020.

changes in anthropogenic radiative forcing and large-scale warming will also induce changes in precipitation. On a global scale the warming increases evaporation, which is balanced by increased precipitation as shown in Fig. 1*B*. The global mean precipitation time series resembles the time series of global mean surface air temperature (Fig. 1*A*), including slow reversals of the upward trends in global precipitation in SSP119 and SSP534OS later in the 21st century.

While the relationship between temperature and precipitation is clear on a global scale, it is more complicated on regional scales, with substantial internal variability and differing regional sensitivities of precipitation to anthropogenic forcing changes. One of the most commonly projected changes in precipitation is a reduction over the Mediterranean (35), as typified by the results in Fig. 2 (the ability of the model to simulate present day Mediterranean precipitation is shown in *SI Appendix*, Fig. S3). There is a clear and persistent downward trend in precipitation in SSP585, with weaker downward trends in the other scenarios, all consistent with many previous results (35). While there is large internal variability of rainfall on regional scales, by using 30-member ensembles we can clearly identify the signals of change. In Fig. 2 we show the results (Fig. 2, *Bottom*) of applying a Kolmogorov–Smirnov two-sided test (*Methods*) to see whether the distributions of simulated rainfall between various pairs of simulations are different. We find (Fig. 2) that after about the year 2000 the simulations with anthropogenic radiative forcing changes are almost all significantly different from the simulations with only natural forcings, with the occasional exception of winter rainfall in SSP119, the scenario with the smallest increase of greenhouse gases.

We focus on results from SSP534OS (and to a lesser extent SSP119) to assess whether the greenhouse gas–induced declines of Mediterranean rainfall are reversible in response to greenhouse gas declines. For SSP534OS and SSP119 Mediterranean rainfall declines during summer (May to October; MJJASO) until the 2050s, after which rainfall increases through the rest of the 21st century (Fig. 2*A*). This midcentury reversal is in response to declining greenhouse gas concentrations in the SSP534OS and SSP119 scenarios (*SI Appendix*, Fig. S1). This demonstrates reversibility of the greenhouse gas–induced summer rainfall decline over the Mediterranean.

In contrast, for the winter half-year (November to April; NDJFMA), we find no such reversal of the Mediterranean precipitation decline in SSP534OS. The downward trend in Mediterranean winter precipitation in SSP534OS occurs when atmospheric CO_2 increases (prior to about 2060) and then continues after 2060 despite reductions in atmospheric CO_2 and associated global cooling. What accounts for such seemingly inconsistent behavior? We show below that the continued reduction in Mediterranean precipitation is attributable to a persistent atmospheric circulation pattern with positive geopotential height anomalies in the western Mediterranean, steering storms away from the Mediterranean and inducing subsidence. What accounts for this atmospheric pattern? We show below that SSP534OS is characterized by a persistently declining and/or weakened strength of the AMOC throughout the 21st century, despite greenhouse gas reductions. The persistently weakened AMOC, through its impact on ocean heat transport, surface temperature, and air–sea interaction, generates an atmospheric teleconnection pattern that generates the anticyclonic circulation over the western Mediterranean, thereby maintaining the long-term decline in winter Mediterranean precipitation. These mechanistic links are explored below.

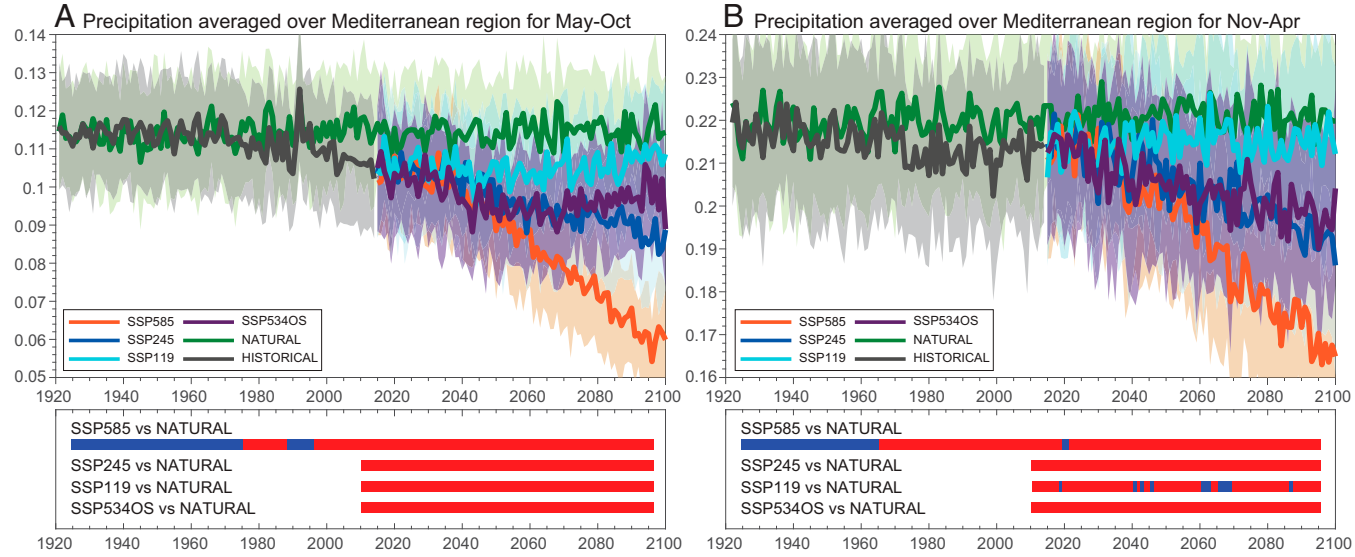

Fig. 2. (*A*) (*Top*) The time series of precipitation (units are cm day^{-1}) averaged over May to October over the Mediterranean (10°W to 38°E, 32°N to 44°N) for various ensembles. Thick solid lines indicate the 30-member ensemble means, while the shaded regions indicate +/- one standard deviation of the departures of the ensemble members from the ensemble mean. (*B*) Same as *A* but for November to April. (*Bottom*) Assessment of when various ensembles differ from the natural ensemble. A sliding 10-y window is used to test whether the distribution of values from either SSP119, SSP245, SSP585, or SSP534OS is significantly different from the corresponding distribution of values from the natural simulation. For example, at year 2026, the distribution formed from all precipitation value for years 2021 to 2031 in the 30 members of the SSP119 simulation (330 values total) is compared to corresponding precipitation values from years 2021 to 2031 from the natural simulation. A two-sided Kolmogorov–Smirnov test (MATLAB routine kstest2) is used to assess whether the distributions are significantly different at the 1% level. If the distributions are different, the appropriate bar is shaded red for year 2026; if not, the bar is shaded blue. Thus, for each pair of experiments (for example, SSP119 versus natural), there is a row with one shaded box per year, where the box is shaded red if the distributions over that 10-y window are significantly different and blue if they are not. Note that for the SSP585 versus natural comparison, years 1921 to 2014 from the historical simulation are combined with years 2015 to 2100 from the SSP585 simulation and then compared to the 1921 to 2100 natural simulation.

Mechanisms of the Persistent Mediterranean Winter Rainfall Decline

To make the connection between a weakened AMOC and Mediterranean rainfall, we first examine the response of the AMOC to changing radiative forcing. The AMOC is a northward flow of warm salty water in the upper layers of the North Atlantic, along with a southward return flow of colder, denser water in deeper layers. The AMOC is important for both oceanic carbon uptake (36) and the global energy balance, transporting ∼1.3 Petawatts (PW) (37) northward. We show an index of the strength of the AMOC at 45°N in Fig. 3 and at 26°N in Fig. 3*B*, which also shows observationally based estimates (details in *Methods*). The model ensemble spread encompasses the observations at 26°N, indicating model consistency with the limited observations. Consistent with many past studies, the simulated AMOC declines in response to increasing greenhouse gases. This decline is linked to freshening and warming of the upper layers of the subpolar North Atlantic, thereby increasing the vertical stability of the water column and inhibiting the deep water formation that is an integral part of the AMOC. The AMOC decline until around 2050 is very similar in all the scenarios (except natural), despite the very different greenhouse gas concentrations in the various scenarios. It is quite striking that in SSP534OS—where global mean temperature peaks in the 2050s and declines thereafter—the AMOC has at best stabilized by the end of the 21st century but has not begun a clear recovery. Even in SSP119, where greenhouse gas concentrations decline over most of the 21st century (starting in 2021 for CH_4 and 2041 for CO_2), the AMOC continues to decline until late in the 21st century, with only a hint of recovery after 2080. For the AMOC, any eventual recovery is many decades delayed relative to when atmospheric greenhouse gases begin to decline (38). The AMOC weakening is tied to enhanced stratification of the upper ocean, and that stratification is not quickly altered (*SI Appendix*, Fig. S4). Enhanced poleward atmospheric water vapor transport in a warmed climate leads to enhanced precipitation at high northern latitudes with resultant enhanced river flow into the North Atlantic and Arctic, leading to freshening of the upper

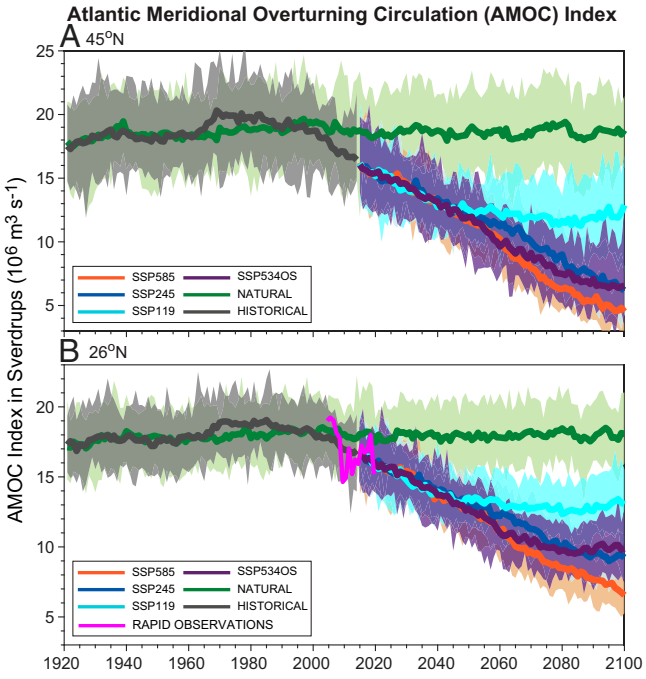

Fig. 3. Time series of indices of the AMOC. Units are Sv. See *Methods* for further details of computing the indices. (*A*) AMOC index at 45°N. (*B*) AMOC index at 26°N. For all time series in *A* and *B* the thick solid lines indicate the 30-member ensemble means, while the shaded regions indicate the range of the ensemble members. The observations in *B* are from the RAPID array at 26°N in the North Atlantic for 2005 to 2019.

ocean. This upper ocean freshening, combined with near-surface warming, reduces upper ocean density and therefore enhances upper ocean stratification. The enhanced upper ocean stratification appears more difficult to reverse than trends in global mean temperature that respond more directly to changes in the net planetary radiative balance.

The enhanced upper ocean stratification inhibits heat transfer from warmer subsurface water to the surface in the Nordic Seas, thereby facilitating cooling and sea ice increases in response to declining greenhouse gases. In addition, the weakened AMOC and associated reduced poleward Atlantic Ocean heat transport contribute to regional cooling and the recovery of Arctic sea ice. We show Arctic sea ice extent for September in Fig. 4*A* and March in Fig. 4*B*. The influence of the greenhouse gas reductions in SSP534OS is quite striking, with a substantial rebound in ice extent by the end of the 21st century. In SSP534OS the September Arctic sea ice extent in 2100 has recovered about 40% of the total loss in sea ice extent that was simulated from the late 20th century to ~2060. The result for SSP534OS is dramatically different from that seen in SSP585 where September sea ice has disappeared by about 2060. A similar recovery of sea ice occurs during March (Fig. 4*B*), with values in SSP534OS returning by the end of the 21st century to values present around 2020 in a few ensemble members with large realizations of internal variability. These results suggest that greenhouse gas reductions comparable to those in SSP534OS would produce a clearly detectable trend of Arctic sea ice recovery by the end of the 21st century (12).

The differing time scales of responses of changes in temperature, AMOC, and Arctic sea ice (*SI Appendix*, Fig. S5) are key components of the mechanism, especially the persistent AMOC decline. The weakened AMOC contributes to rapidly expanding Arctic sea ice, especially during winter (Fig. 4*B* and *SI Appendix*, Fig. S5). Moreover, the rapidly expanding sea ice in SSP534OS enhances regional cooling of near-surface air temperature, especially over the subpolar North Atlantic in winter where the growing sea ice inhibits warming of the near-surface atmosphere from the ocean. We show the change in near-surface air temperature in SSP534OS over the second half of the 21st century (2081 to 2100 minus 2046 to 2065) for NDJFMA (Fig. 5*A*) and MJJASO (Fig. 5*B*). There is strong regional cooling, with maximum amplitude in the subpolar North Atlantic and Arctic during NDJFMA. This cooling is a result of the greenhouse gas reductions but is also amplified by the rapidly expanding sea ice that is enhanced by the persistently weakened AMOC. This very strong winter cooling over the subpolar North Atlantic and Arctic creates an anomalous cyclonic circulation in the midtroposphere (Fig. 5*C*). Emanating from this strong cyclonic circulation is an atmospheric teleconnection pattern with positive geopotential height anomalies over the western Mediterranean. It is this anticyclonic atmospheric circulation over the Mediterranean region that creates subsidence over the Mediterranean, inhibits cyclonic storms, and continues the long-term precipitation decline—despite significant reductions in greenhouse gases. During summer, there is cooling over the subpolar North Atlantic, but this cooling only generates a modest atmospheric circulation response that is not enough to generate a strong atmospheric teleconnection over the Mediterranean and impede the recovery of summer precipitation over the Mediterranean.

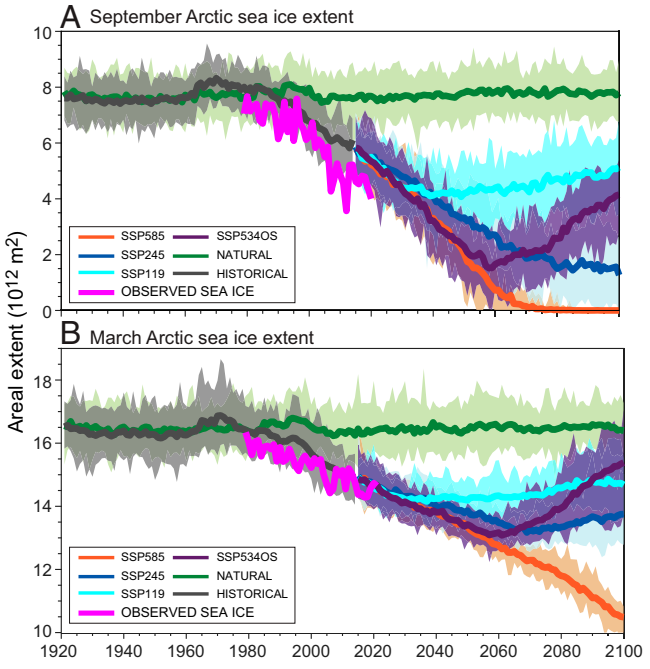

Fig. 4. (*A*) Time series of Arctic sea ice extent in September. Units are 10^{12} m^2. (*B*) Same as *A* but for March. For all time series in *A* and *B* the thick solid lines indicate the 30-member ensemble means, while the shaded regions indicate the range of the ensemble members. Observed sea ice extent from Fetterer et al. (51).

We test the role of the AMOC in Mediterranean rainfall recovery using an additional nine-member ensemble of simulations called SSP534OS_STRONG_AMOC. This additional ensemble is identical to SSP534OS, except that we artificially strengthen the AMOC by removing fresh water from the surface layer of the ocean over the subpolar North Atlantic (*Methods*). The fresh water removal increases upper ocean salinity and density in the subpolar North Atlantic, thereby artificially strengthening deep water formation and the AMOC. We postulated above that the continued decline of Mediterranean winter rainfall despite greenhouse gas reductions is influenced by a persistently weakened AMOC. Through this experimental design we can isolate the role of the AMOC and test whether the Mediterranean winter rainfall decline seen in SSP534OS would still occur with a stronger AMOC by comparing the results of SSP534OS_STRONG_AMOC to SSP534OS. This additional ensemble of simulations starts from 1 January 2041, with initial conditions from SSP 534OS, and extends to 2100.

We show time series of the AMOC indices from SSP534OS and SSP534OS_STRONG_AMOC in Fig. 6*A*. In contrast to the ongoing AMOC decline in SSP534OS (black line), the AMOC in SSP534OS_STRONG_AMOC clearly strengthens (red line), returning to 20th century values within 2 to 3 decades. The strengthened AMOC enhances poleward oceanic heat transport, leading to warming over the Northern Hemisphere with largest amplitude over the Nordic Seas (Fig. 6*B*), positive atmospheric geopotential height anomalies over the North Atlantic subpolar gyre (Fig. 6*C*), and an atmospheric teleconnection pattern that results in cyclonic circulation over the Mediterranean (Fig. 6*C*) and increased winter Mediterranean rainfall (Fig. 6*D*). In the SSP534OS_STRONG_AMOC simulations with a strengthening AMOC, winter precipitation over the Mediterranean increases in the late 21st century (Fig. 6*D*), opposite to the trend in SSP534OS with a weakening AMOC. Note how the 500-hPa geopotential response to the strengthened AMOC (Fig. 6*C*) is almost the mirror image of the 500-hPa geopotential height changes in the SSP534OS simulation between the late and mid-21st century periods (Fig. 5*C*). This supports the hypothesis that the AMOC changes, through their impact on air–sea interaction and surface air temperature in the subpolar North Atlantic, can

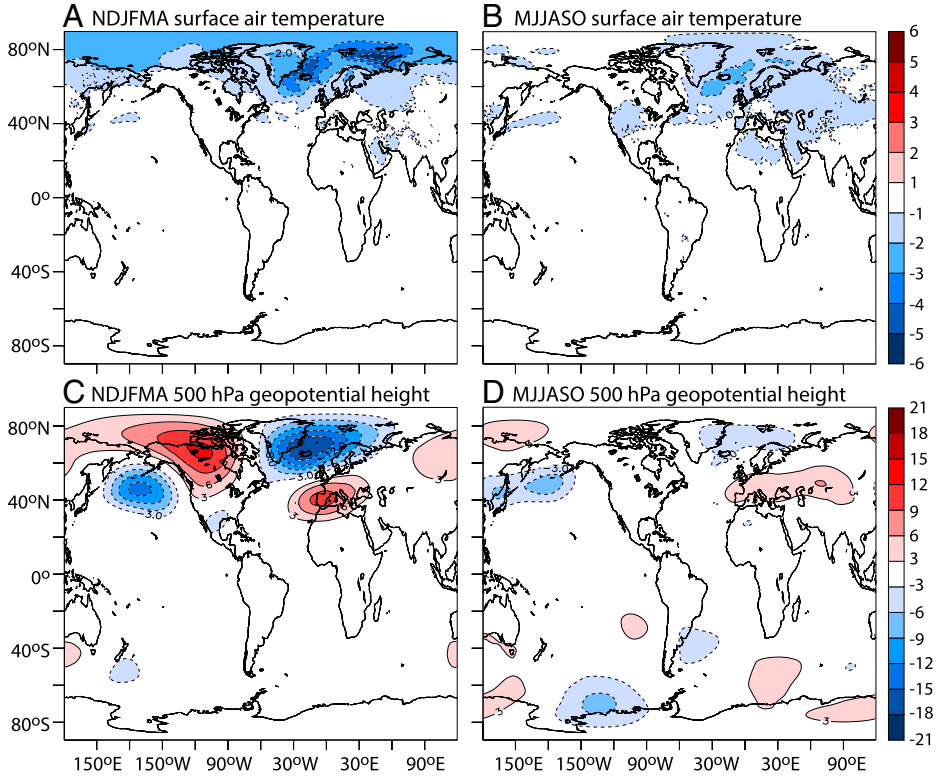

Fig. 5. Differences for (*A* and *B*) surface air temperature and (*C* and *D*) 500 hPa geopotential height for experiment SSP534OS. The differences are calculated as the mean over 2081 to 2100 minus the mean over 2046 to 2065. Units for temperature are °C and meters for 500 hPa geopotential height. For geopotential height the zonal mean was removed prior to plotting in order to accentuate regional structures. (*A*) Difference in surface air temperature for November to April (NDJFMA). (*B*) Same as *A* but for May to October (MJJASO). (*C*) Difference in 500 hPa geopotential height (NDJFMA). (*D*) Same as *C* but for MJJASO.

induce large-scale atmospheric teleconnections with significant regional climate change impacts.

The persistence of the weakened AMOC in SSP534OS appears to be the source of the continued drying over the Mediterranean despite reductions in atmospheric CO_2. This result suggests that the long time scales of ocean circulation response may have important and counterintuitive atmospheric impacts, so that aspects of climate change may not be rapidly reversed by reducing atmospheric CO_2. Given the central importance of the prolonged weakened state of the AMOC to the results shown here, it is crucial to assess whether the persistently weakened AMOC under the SSP534OS scenario is unique to the SPEAR model used here. We have examined several models that have contributed SSP534OS simulations to the CMIP6 archives. The small number of such simulations available makes firm conclusions difficult, but we find that at least one model [Community Earth System Model version 2-Whole Atmosphere Community Climate Model, CESM2-WACCM (39)] has changes in the AMOC, atmospheric circulation, and precipitation that resemble the results in SPEAR (*SI Appendix*, Fig. S6). However, previous results (14) examining the response to idealized rates of CO_2 increase and decrease have found a much closer correspondence of the AMOC to the CO_2 forcing, without the substantial persistence of the weakened AMOC state found in the present study. It will be crucial to better understand the sources of any differences in models regarding the long-term response of the AMOC and its relevance for reversing aspects of climate change.

Discussion

As the impacts of climate change continue to grow, there is an increasing need for improved projections—not only of how the climate system will change but of pathways and strategies to mitigate the impact of projected changes and to potentially reverse changes that have occurred. We have used large ensembles of a climate model subjected to a variety of future trajectories of anthropogenic drivers of climate change to probe future climates, especially regarding how rapidly various aspects of climate change are reversible in response to possible future climate change mitigation. We find that atmospheric temperature and Arctic sea ice cover (12) respond relatively quickly and directly to reductions in greenhouse gas concentrations. However, other aspects of the climate system, such as the AMOC, either continue to weaken or fail to recover even with significant reductions of greenhouse gases in the 21st century.

Consistent with many studies, in our simulations we find that precipitation over the Mediterranean declines in response to increasing greenhouse gases. However, we find that the decline in winter precipitation continues even after substantial reductions in greenhouse gases later in the 21st century. This apparent contradiction is explained in these simulations by a persistently weakened AMOC that, in concert with cooling and sea ice growth over the subpolar North Atlantic, induces atmospheric circulation changes with cyclonic circulation over the subpolar North Atlantic and anticyclonic flow over the Mediterranean. This persistent atmospheric circulation over the Mediterranean sustains the long-term decline of winter precipitation, even when atmospheric CO_2 is reduced. This is an example of a "surprise" in the climate system; in this case, a persistent change in one component of the climate system (the AMOC) appears to inhibit the recovery of another component of the climate system (Mediterranean winter precipitation) despite significant reductions in atmospheric greenhouse gases. This surprise is the result of an asymmetry. For the ensemble of simulations with SSP534OS forcing, the increasing greenhouse gases (until around 2060) occur in a climate with a strong to moderate AMOC. In contrast, the middle to late 21st century greenhouse gas declines occur in a climate with a persistently weak AMOC. The asymmetry in the Mediterranean winter precipitation response to greenhouse

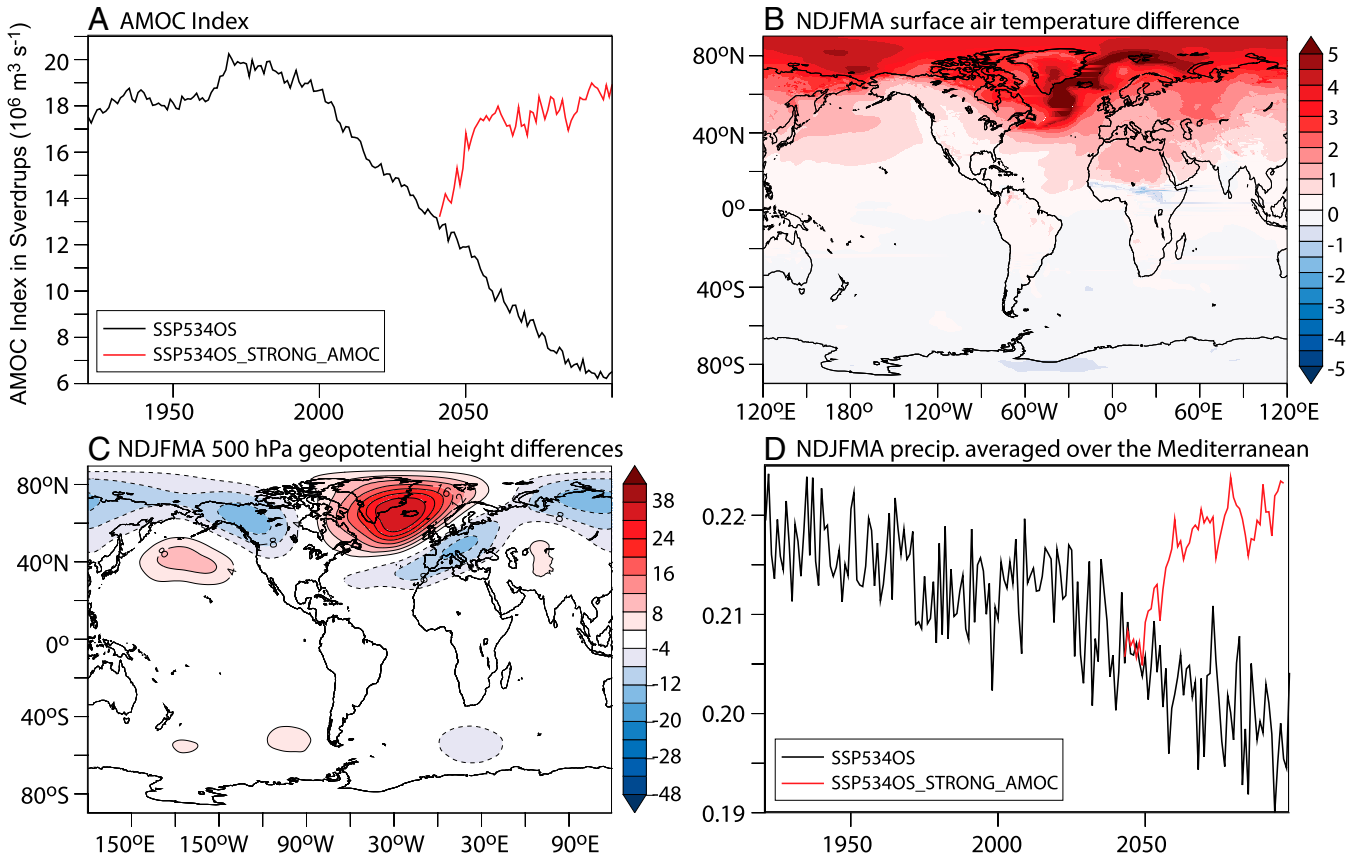

Fig. 6. Results from an ensemble of simulations called "SSP534OS_STRONG_AMOC" (described in main text and in *Mechanisms of the Persistent Mediterranean Winter Rainfall Decline*). This tests the linkage between AMOC strength and the response of Mediterranean winter precipitation to greenhouse gas changes. (*A*) Indices of the AMOC at 45°N for SSP534OS (black) and SSP534OS_STRONG_AMOC (red). (*B*) Difference in winter (NDJFMA) surface air temperature for 2081 to 2100 for SSP534OS_STRONG_AMOC minus SSP534OS. Units are °C. (*C*) Same as *B* but for 500 hPa geopotential height. Units are meters. (*D*) Winter (NDJFMA) precipitation averaged over the Mediterranean for SSP534OS (black) and SSP534OS_STRONG_AMOC (red). Units are cm day^{-1}.

gas increases and decreases is traceable to the failure of the AMOC to rapidly recover as greenhouse gases decline, thereby creating the asymmetry. This suggests that the rate at which the AMOC recovers in response to decreasing greenhouse gases is an important influence on potential future climate system recovery. It will be important to better understand differences in the rate of AMOC recovery that are simulated by different models.

These results suggest that even substantial climate mitigation efforts may only be sufficient to achieve a partial climate recovery in this century (9). Aspects of the climate system that are most directly tied to the energy balance of the planet, such as surface temperature (40) and Arctic sea ice, appear to alter their trajectories in direct response to the reductions in greenhouse gas concentrations. Even so, in none of the scenarios does global mean surface air temperature return to year 2000 values by the end of the 21st century.

In addition, on regional scales, any responses to emissions reductions can be difficult to clearly identify due to the strong role of internal variability (7). We have used 30-member ensembles to achieve results that are statistically significant (as shown in Fig. 2), but the statistical significance becomes much weaker or even vanishes on regional scales with smaller ensembles. This presents a challenge for robustly assessing and confidently attributing the impacts of potential future greenhouse gas reductions on regional-scale climate as any forced impacts are enmeshed in strong internal variability on decadal scales.

The climate model used in this study has a relatively fine atmosphere–land resolution of 50 km, which is very helpful for studies of regional climate and extremes. An additional advantage of this model (and a lower-resolution version) is that it is used for real-time seasonal to decadal prediction, and thus, its skill in predicting temperature, sea ice, and the AMOC is continuously assessed. However, the model ocean component has a horizontal resolution of ~100 km and does not explicitly resolve small-scale oceanic processes, such as mesoscale eddies or important topographically constrained flows. Since our results concerning Mediterranean rainfall reversibility were heavily influenced by future AMOC behavior, it is important to assess the robustness of the current results by evaluating similar simulations with other models, including those with finer ocean resolution (41–43). While almost all models project a weakening of the AMOC in response to increasing greenhouse gases, there is a wide range in the amplitude and timing of such weakening and associated climatic impacts (38, 44). Such differences, as well as characteristics of ocean–atmosphere interactions, may influence the robustness of the mechanism identified here where the AMOC inhibits recovery of Mediterranean winter rainfall. Additional radiative forcings are also critical for the future evolution of Mediterranean precipitation (45).

More generally, one can speculate as to whether the current classes of climate models in wide use are too linear in their behavior. Are there other important phenomena or processes in the real climate system—possibly not well represented in current models—that also inhibit the recovery of the climate system even with significant climate change mitigation efforts? Such questions are vital to quantify climate risk and inform planning decisions (46). To the extent that nonlinearities and threshold behaviors exist that are not captured in current

climate models, we may be systematically underestimating the risk from climate change and overestimating our ability to reverse such change once it occurs.

Methods

Model and Primary Simulations. We conduct 30-member ensembles of simulations using the Geophysical Fluid Dynamics Laboratory (GFDL) SPEAR model (47). The model has an atmosphere–land resolution of ∼50 km and an ocean–ice resolution of ∼100 km. The first ensemble (historical) runs from 1921 through 2014. Initial conditions for the atmosphere, ocean, and sea ice are taken from points 20 y apart in a long control simulation that has constant 1850 atmospheric composition. The land initial conditions for year 1921 are the same in all members and are taken from a single transient simulation of the model that extended from 1851 to 1920. This process saved computer time by not requiring all ensemble members to start in year 1851. The model is forced over the period 1921 to 2014 with observed estimates of changes in greenhouse gases and aerosols, land use (48), solar irradiance, and volcanic aerosols (49).

A second ensemble (natural) starts from the same 1921 initial conditions as the historical ensemble but is forced only with radiative forcing changes from natural sources–solar irradiance and volcanic aerosols. All other radiative forcing components (greenhouse gases, anthropogenic aerosols, and land use) are kept fixed at 1921 values. The natural ensemble runs from 1921 to 2100. For the period 1921 to 2014, observational estimates of changes in volcanic aerosols and solar irradiance are used. For the period 2015 to 2100 a synthetic estimate of solar irradiance changes is used based on the observed solar cycle. Volcanic aerosols after 2024 are set to values derived as the long-term mean over 1851 to 2014, with a linear transition from observed values in 2014 to the prescribed values after 2024.

Four additional ensembles are run from 2015 through 2100 and use various projections of future radiative forcing changes (49) (*SI Appendix*, Fig. S1 for CO_2 and CH_4 concentrations in the scenarios). Ensemble SSP585 uses forcings from the SSP5-8.5 scenario and contains the largest increases in radiative forcing and therefore the largest warming. Ensemble SSP245, using forcings from the SSP2-4.5 scenario, has smaller total increases in radiative forcing. SSP119 uses the SSP1-1.9 radiative forcings and has the smallest increase in future radiative forcing changes. Ensemble SSP534OS uses the SSP5-3.4OS forcing, which is very similar to SSP5-8.5 until the year 2040; after 2040, there is a rapid decline in greenhouse gas emissions and other drivers, resulting in negative emissions after around 2070. The time series of the net radiative balance at the top of the atmosphere are shown in *SI Appendix*, Fig. S2.

All ensembles described above have 30 members, and this allows an assessment of the radiatively forced signal of climate change (evaluated as the ensemble mean over all 30 members) as well as a measure of the uncertainty due to internal variability of the system, indicated by the spread of the 30 ensemble members around the ensemble mean.

Additional Simulation to Assess AMOC Impact on Mediterranean Winter Precipitation Trends. We conduct an additional nine-member ensemble of simulations that are identical to SSP534OS except that we remove fresh water from the subpolar gyre and Nordic Seas to artificially strengthen the AMOC. We refer to this set as SSP534OS_STRONG_AMOC. The additional simulations start from conditions on 1 January 2041, from the first nine members of the SSP534OS ensemble, and the simulations extend through 2100. The total rate of fresh water removal (applied uniformly over the Atlantic between 50°N and 80°N) is 0.1 sverdrups (Sv; 1 Sv = 10^6 m^3 s^{-1}). By removing fresh water, we increase upper ocean salinity and density, thereby reducing upper ocean stratification, enhancing deep water formation, and strengthening the AMOC. The removed fresh water is no longer accounted for in the system and is used purely as an artificial technique to strengthen the AMOC to allow an assessment of the role of the AMOC. In these additional simulations the AMOC returns to typical 20th century strength after 2 to 3 decades. By comparing SSP534OS_STRONG_AMOC and SSP534OS we can evaluate the impact of a strong or weak AMOC on whether greenhouse gas reductions can reverse the Mediterranean winter rainfall decline.

Ocean Circulation Indices. We compute indices of the AMOC. We first calculate the zonal integral across the Atlantic basin of the meridional volume transport in isopycnal coordinates. Meridional stream function values are then computed at each level by taking an indefinite integral of the zonally integrated transport from the top of the ocean to that level. We define an AMOC index at individual latitudes as the maximum value of the stream function across a range of density levels. We compute indices at 45°N and 26°N. The latter index can be compared directly to observations through the Rapid Climate Change - Atlantic Meridional Overturning Program (RAPID-AMOC).

Observational Data. The observationally based record of the AMOC is from the Rapid Climate Change - Atlantic Meridional Overturning Circulation Program (RAPID-AMOC) (50) (downloaded 17 May 2022). Observed sea ice data were downloaded from the National Snow and Ice Data Center (51) (https://nsidc.org/data/g02135, downloaded 30 May 2021). The Climatic Research Unit Temperature dataset version 5 (CRUTEM5) and the Met Office Hadley Centre/Climatic Research Unit dataset version 5 (HadCRUT5) observational temperature (52) datasets were downloaded from https://crudata.uea.ac.uk/cru/data/temperature/ on 6 July 2021. The Goddard Institute for Space Studies (GISS) surface temperature (53) dataset (GISTEMP v4) was downloaded on 6 July 2021.

Data, Materials, and Software Availability. Model output used in the analyses can be found at https://doi.org/10.5281/zenodo.6954827 (54). The observationally based record of the AMOC is from the RAPID Program (https://rapid.ac.uk/rapidmoc/, downloaded 17 May 2022) (55). Observed sea ice data were downloaded from the National Snow and Ice Data Center (https://nsidc.org/data/g02135, downloaded 30 May 2021) (56). The CRUTEMP and HadCRUT5 observational temperature datasets were downloaded from https://crudata.uea.ac.uk/cru/data/temperature/ on 6 July 2021 (57). The GISS surface temperature dataset (GISTEMP v4) was downloaded on 6 July 2021. The Modular Ocean Model version 6 code is publicly available at https://github.com/NOAA-GFDL (58). Source code for the atmosphere component used in SPEAR is available at https://data1.gfdl.noaa.gov/nomads/forms/am4.0/ (59).

ACKNOWLEDGMENTS. We thank three anonymous reviewers and the Editor, as well as Drs. Robert Hallberg and P. C. D. Milly, for extremely useful comments on earlier versions of this manuscript. Data from the RAPID AMOC monitoring project are funded by the Natural Environment Research Council and are freely available from https://rapid.ac.uk/rapidmoc/. Support for this project, including for high-performance computing, was through base funding of GFDL provided by the National Oceanic and Atmospheric Administration.

Author affiliations: [a]Geophysical Fluid Dynamics Laboratory, National Oceanic and Atmospheric Administration, Princeton, NJ 08540; and [b]University Corporation for Atmospheric Research, Boulder, CO 80307

1. S. I. Seneviratne, M. Hauser, Regional climate sensitivity of climate extremes in CMIP6 versus CMIP5 multimodel ensembles. *Earths Futur.* **8**, EF001474 (2020).
2. F. E. L. Otto *et al.*, Anthropogenic influence on the drivers of the Western Cape drought 2015–2017. *Environ. Res. Lett.* **13**, 124010 (2018).
3. N. S. Diffenbaugh, D. L. Swain, D. Touma, Anthropogenic warming has increased drought risk in California. *Proc. Natl. Acad. Sci. U.S.A.* **112**, 3931–3936 (2015).
4. D. L. Swain, B. Langenbrunner, J. D. Neelin, A. Hall, Increasing precipitation volatility in twenty-first-century California. *Nat. Clim. Chang.* **8**, 427–433 (2018).
5. R. A. Betts *et al.*, Changes in climate extremes, fresh water availability and vulnerability to food insecurity projected at 1.5°C and 2°C global warming with a higher-resolution global climate model. *Philos. Trans. R. Soc. Math. Phys. Eng. Sci.* **376**, 20160452 (2018).
6. J.-L. Martel, A. Mailhot, F. Brissette, Global and regional projected changes in 100-yr subdaily, daily, and multiday precipitation extremes estimated from three large ensembles of climate simulations. *J. Clim.* **33**, 1089–1103 (2020).
7. C. Tebaldi, P. Friedlingstein, Delayed detection of climate mitigation benefits due to climate inertia and variability. *Proc. Natl. Acad. Sci. U.S.A.* **110**, 17229–17234 (2013).
8. B. H. Samset, J. S. Fuglestvedt, M. T. Lund, Delayed emergence of a global temperature response after emission mitigation. *Nat. Commun.* **11**, 3261 (2020).
9. S. Solomon, G.-K. Plattner, R. Knutti, P. Friedlingstein, Irreversible climate change due to carbon dioxide emissions. *Proc. Natl. Acad. Sci. U.S.A.* **106**, 1704–1709 (2009).
10. I. M. Held *et al.*, Probing the fast and slow components of global warming by returning abruptly to preindustrial forcing. *J. Clim.* **23**, 2418–2427 (2010).
11. N. P. Gillett, V. K. Arora, K. Zickfeld, S. J. Marshall, W. J. Merryfield, Ongoing climate change following a complete cessation of carbon dioxide emissions. *Nat. Geosci.* **4**, 83–87 (2011).
12. K. C. Armour, I. Eisenman, E. Blanchard-Wrigglesworth, K. E. McCusker, C. M. Bitz, The reversibility of sea ice loss in a state-of-the-art climate model. *Geophys. Res. Lett.* **38**, L16705 (2011).
13. K. Zickfeld *et al.*, Long-term climate change commitment and reversibility: An emic intercomparison. *J. Clim.* **26**, 5782–5809 (2013).

14. P. Wu, J. Ridley, A. Pardaens, R. Levine, J. Lowe, The reversibility of CO_2 induced climate change. *Clim. Dyn.* **45**, 745–754 (2015).
15. O. Boucher *et al.*, Reversibility in an Earth System model in response to CO_2 concentration changes. *Environ. Res. Lett.* **7**, 024013 (2012).
16. M.-A. Sun *et al.*, Reversibility of the hydrological response in East Asia from CO_2-derived climate change based on CMIP6 simulation. *Atmosphere* **12**, 72 (2021).
17. T. J. W. Wagner, I. Eisenman, How climate model complexity influences sea ice stability. *J. Clim.* **28**, 3998–4014 (2015).
18. D. Ehlert, K. Zickfeld, Irreversible ocean thermal expansion under carbon dioxide removal. *Earth Syst. Dyn.* **9**, 197–210 (2018).
19. K. Zickfeld, S. Solomon, D. M. Gilford, Centuries of thermal sea-level rise due to anthropogenic emissions of short-lived greenhouse gases. *Proc. Natl. Acad. Sci. U.S.A.* **114**, 657–662 (2017).
20. J. Garbe, T. Albrecht, A. Levermann, J. F. Donges, R. Winkelmann, The hysteresis of the Antarctic Ice Sheet. *Nature* **585**, 538–544 (2020).
21. J. M. Gregory, S. E. George, R. S. Smith, Large and irreversible future decline of the Greenland ice sheet. *Cryosphere* **14**, 4299–4322 (2020).
22. M. Collins *et al.*, "Long-term climate change: Projections, commitments and irreversibility" in *Climate Change 2013: The Physical Science Basis. Contribution of Working Group I to the Fifth Assessment Report of the Intergovernmental Panel on Climate Change*, T. F. Stocker *et al.*, eds. (Cambridge University Press, Cambridge, United Kingdom, 2013). pp. 1029–1136.
23. K. Zickfeld, D. Azevedo, S. Mathesius, H. D. Matthews, Asymmetry in the climate–carbon cycle response to positive and negative CO_2 emissions. *Nat. Clim. Chang.* **11**, 613–617 (2021).
24. K. A. McKinnon, C. Deser, Internal variability and regional climate trends in an observational large ensemble. *J. Clim.* **31**, 6783–6802 (2018).
25. C. Deser *et al.*, Insights from Earth system model initial-condition large ensembles and future prospects. *Nat. Clim. Chang.* **10**, 277–286 (2020).
26. N. Maher *et al.*, The Max Planck Institute grand ensemble: Enabling the exploration of climate system variability. *J. Adv. Model. Earth Syst.* **11**, 2050–2069 (2019).
27. M. Hoerling *et al.*, On the increased frequency of Mediterranean drought. *J. Clim.* **25**, 2146–2161 (2012).
28. J. Y. Lee *et al.*, "Future global climate: Scenario-based projections and near-term information" in *Climate Change 2021: The Physical Science Basis. Contribution of Working Group I to the Sixth Assessment Report of the Intergovernmental Panel on Climate Change*. V. Masson-Delmotte *et al.*, *Eds*, (Cambridge University Press, Cambridge, United Kingdom, 2021). pp. 553–672.
29. B. P. Kirtman *et al.*, The North American multimodel ensemble: Phase-1 seasonal-to-interannual prediction; Phase-2 toward developing intraseasonal prediction. *Bull. Am. Meteorol. Soc.* **95**, 585–601 (2014).
30. X. Yang *et al.*, On the development of GFDL's decadal prediction system: Initialization approaches and retrospective forecast assessment. *J. Adv. Model. Earth Syst.* **13**, e2021MS002529 (2021).
31. F. Lu *et al.*, GFDL's SPEAR seasonal prediction system: Initialization and Ocean Tendency Adjustment (OTA) for coupled model predictions. *J. Adv. Model. Earth Syst.* **12**, e2020MS002149 (2020).
32. Y. Zhang *et al.*, Mechanisms of Regional Arctic Sea ice predictability in two dynamical seasonal forecast systems. *J. Clim.* **35**, 1–63 (2022).
33. K. Riahi *et al.*, The shared socioeconomic pathways and their energy, land use, and greenhouse gas emissions implications: An overview. *Glob. Environ. Change* **42**, 153–168 (2017).
34. Z. Hausfather, G. P. Peters, Emissions–The 'business as usual' story is misleading. *Nature* **577**, 618–620 (2020).
35. A. Tuel, E. A. B. Eltahir, Why is the Mediterranean a climate change hot spot? *J. Clim.* **33**, 15 (2020).
36. A. Katavouta, R. G. Williams, Ocean carbon cycle feedbacks in CMIP6 models: Contributions from different basins. *Biogeosciences* **18**, 3189–3218 (2021).
37. W. E. Johns *et al.*, Continuous, array-based estimates of Atlantic Ocean heat transport at 26.5°N. *J. Clim.* **24**, 2429–2449 (2011).
38. J. B. Palter, T. L. Frölicher, D. Paynter, J. G. John, Climate, ocean circulation, and sea level changes under stabilization and overshoot pathways to 1.5 K warming. *Earth Syst. Dyn.* **9**, 817–828 (2018).
39. G. Danabasoglu, NCAR CESM2-WACCM model output prepared for CMIP6 CMIO. Version 20220208 (Earth System Grid Federation, 2019). https://doi.org/10.22033/ESGF/CMIP6.10024. Accessed 9 February 2022.
40. C. Tebaldi *et al.*, Climate model projections from the Scenario Model Intercomparison Project (ScenarioMIP) of CMIP6. *Earth Syst. Dyn.* **12**, 253–293 (2021).
41. L. C. Jackson *et al.*, Impact of ocean resolution and mean state on the rate of AMOC weakening. *Clim. Dyn.* **55**, 1711–1732 (2020).
42. M. J. Roberts *et al.*, Sensitivity of the Atlantic Meridional overturning circulation to model resolution in CMIP6 HighResMIP simulations and implications for future changes. *J. Adv. Model. Earth Syst.* **12**, e2019MS002014 (2020).
43. W. Weijer, W. Cheng, O. A. Garuba, A. Hu, B. T. Nadiga, CMIP6 models predict significant 21st century decline of the Atlantic Meridional overturning circulation. *Geophys. Res. Lett.* **47**, e2019GL086075 (2020).
44. K. Bellomo, M. Angeloni, S. Corti, J. von Hardenberg, Future climate change shaped by inter-model differences in Atlantic meridional overturning circulation response. *Nat. Commun.* **12**, 3659 (2021).
45. T. Tang *et al.*, Dynamical response of Mediterranean precipitation to greenhouse gases and aerosols. *Atmos. Chem. Phys.* **18**, 8439–8452 (2018).
46. D. P. Keller *et al.*, The Carbon Dioxide Removal Model Intercomparison Project (CDRMIP): Rationale and experimental protocol for CMIP6. *Geosci. Model Dev.* **11**, 1133–1160 (2018).
47. T. L. Delworth *et al.*, SPEAR: The next generation GFDL modeling system for seasonal to multidecadal prediction and projection. *J. Adv. Model. Earth Syst.* **12**, e2019MS001895 (2020).
48. G. C. Hurtt *et al.*, Harmonization of global land use change and management for the period 850–2100 (LUH2) for CMIP6. *Geosci. Model Dev.* **13**, 5425–5464 (2020).
49. M. Meinshausen *et al.*, Historical greenhouse gas concentrations for climate modelling (CMIP6). *Geosci. Model Dev.* **10**, 2057–2116 (2017).
50. E. Frajka-Williams *et al.*, Atlantic meridional overturning circulation observed by the RAPID-MOCHA-WBTS (RAPID-Meridional Overturning Circulation and Heatflux Array-Western Boundary Time Series) array at 26N from 2004 to 2020 (v2020.1) (British Oceanographic Data Centre, Natural Environment Research Council, United Kingdom, 2021), 10.5285/cc1e34b3-3385-662b-e053-6c86abc03444.
51. F. Fetterer, K. Knowles, W. Meier, M. Savoie, A. Windnagel, Sea Ice Index, version 3 (National Snow and Ice Data Center, 2017). https://doi.org/10.7265/N5K072F8. Accessed 30 May 2021, via ftp.sidads.colorado.edu.
52. C. P. Morice *et al.*, An updated assessment of near-surface temperature change from 1850: The HadCRUT5 data set. *J. Geophys.* Res. **126**, e2019JD032361 (2021).
53. N. J. L. Lenssen *et al.*, Improvements in the GISTEMP uncertainty model. *J. Geophys. Res.* **124**, 6307–6326 (2019).
54. T. Delworth, Data associated with PNAS Delworth et al 2022. Zenodo. https://zenodo.org/record/6954827#.YvJbuhxByUk. Deposited 3 August 2022.
55. T. L. Delworth, A weakened AMOC may prolong greenhouse gas–induced Mediterranean drying even with significant and rapid climate change mitigation. RAPID. https://rapid.ac.uk/rapidmoc/. Accessed 17 May 2022.
56. T. L. Delworth, Sea Ice Index, Version 3 (G02135). National Snow and Ice Data Center. https://nsidc.org/data/g02135/versions/3. Accessed 30 May 2021.
57. T. L. Delworth, CRUTEMP and HadCRUT5 observational temperature datasets. https://crudata.uea.ac.uk/cru/data/temperature/. Accessed 6 July 2021.
58. T. L. Delworth, Modular Ocean Model version 6. GitHub. https://github.com/NOAA-GFDL/MOM6. Accessed 11 August 2022.
59. T. L. Delworth, Source code for the atmosphere component used in SPEAR. https://data1.gfdl.noaa.gov/nomads/forms/am4.0/. Accessed 11 August 2022.